PERIODICO di MINERALOGIA
established in 1930

Dipartimento di Scienze della Terra
Sapienza Università di Roma

An International Journal of
Mineralogy, Crystallography, Geochemistry,
Ore Deposits, Petrology, Volcanology
and applied topics on Environment, Archaeometry and Cultural Heritage

Thermally induced behavior of the K-exchanged erionite: a further step in understanding the structural modifications of the erionite group upon heating

Paolo Ballirano [1,2], Andrea Bloise [3], Carlo Cremisini [4], Elisa Nardi [4], Maria Rita Montereali [4], Alessandro Pacella [1,*]

[1] Department of Earth Sciences, Sapienza University of Rome, P.le A. Moro 5, I-00185 Rome, Italy
[2] Rectorial Laboratory Fibres and Inorganic Particulate, Sapienza University of Rome, P.le A. Moro 5, I-00185 Rome, Italy
[3] Department of Biology, Ecology and Earth Sciences, University of Calabria, Via Pietro Bucci, I-87036 Rende, CS, Italy
[4] ENEA, Casaccia Research Centre, via Anguillarese 301, S. Maria di Galeria, I-00123 Rome, Italy

ARTICLE INFO

Submitted: December 2017
Accepted: April 2018
Available on line: May 2018

* Corresponding author:
alessandro.pacella@uniroma1.it

DOI: 10.2451/2018PM769

How to cite this article:
Ballirano P. et al. (2018)
Period. Mineral. 87, xx-xx

ABSTRACT

Fibrous erionite is a naturally occurring zeolite considered to be highly carcinogenic upon inhalation, even more than crocidolite. Since no iron is typically present in erionite, its toxicity has been attributed to ion-exchanged Fe participating in Fenton chemistry. Recently, a study aimed at investigating possible fiber inactivation routes surprisingly showed that, despite having completely occluded all available pores with K ions, the erionite-Na sample preserved the property to upload Fe (II) within the structure. In this work, the thermal behavior of the K-exchanged erionite-Na was investigated by TG/DSC and *in situ* XRPD analyses in order to provide relevant information for modeling the thermally induced behavior of the erionite group. Rietveld refinement results evidenced a general trend of cell parameters and volume with temperature similar to that observed for erionite-K from Rome (Oregon, USA). However, the dependence of T_{dehydr} and T_{break} from Si/Si+Al ratio observed in zeolites (high Si content favours a lower T_{dehydr} and a higher T_{break}) is not observed, possibly due to the effect of the relevant amount of large K ions dispersed within the erionite cage, acting as reinforcing blocks for the framework. Heating produces a progressive emptying of the Ca sites, common effect previously observed in erionite samples showing different chemistry. In addition, K1 *s.s.* remains unchanged evidencing the absence of any "internal ion exchange" process, whereas *s.s.* at K2 increases in the range 438-573 K and then slowly decreases in the range 700-1218 K. Both Rietveld and DSC data suggest the motion of K ions from OW sites toward the walls of the erionite cavity during dehydration.

Keywords: K-exchanged erionite; TG/DSC analyses; *in situ* X-ray powder diffraction; Rietveld method; thermal behaviour.

INTRODUCTION

Erionite (ERI) is a zeolite, often characterized by fibrous morphology, that crystallizes in the hexagonal crystal system, space group $P6_3/mmc$ (Kawahara and Curien, 1969). It occurs naturally and its average formula is $K_2(Na,Ca_{0.5})_8[Al_{10}Si_{26}O_{72}]\cdot 30H_2O$ (Coombs et al., 1997). Erionite has a large chemical variability (Wise and Tschernich, 1976; Passaglia et al., 1998; Gualtieri et al., 1998) and it is classified as erionite-K, -Na, and -Ca (Coombs et al., 1997) according to the most abundant

extraframework (EF) cation. From the structural point of view, it pertains to the so-called ABC-6 family (Gottardi and Galli, 1985). The erionite framework contains columns of alternating cancrinite (e) cages, and double 6-rings (D6R). The erionite cavities are formed by the linking at the same level, via single 6-rings, of e cages pertaining to adjacent columns (Staples and Gard, 1959; Gard and Tait, 1973). The unit cell hosts two cancrinite cages and two D6R alternating along 0, 0, *z*, and two erionite cages running along 1/3, 2/3, *z*, and 2/3, 1/3, *z*, respectively. Following the ABC-6 scheme, layers consisting of 6-membered rings of TO_4 tetrahedra (T=Si, Al), are stacked along the *z*-direction, according to an AABAAC sequence. In theory, there are 10 different sequences for a period of six-layers (Meier and Groner, 1981; Smith and Bennett, 1981), but only four of them occur in nature: AABAAC, erionite, AABBCC, chabazite (Smith et al., 1963), ABBACC, bellbergite (Rüdinger et al., 1993), and ABABAC, liottite (Ballirano et al., 1996).

The cancrinite and erionite cages host the EF cations and H_2O. The small e cage hosts a potassium ion at its center (K1 site). The large erionite cavity contains four cation sites, labeled Ca1, Ca2, Ca3, and Mg, residing at or near the axis of the cavity (Alberti et al., 1997; Gualtieri et al., 1998; Ballirano et al., 2009). K-rich erionite samples show a further EF cation site, labeled K2, located near the walls of the erionite cavity (Schlenker et al., 1977; Gualtieri et al., 1998; Ballirano et al., 2009). The EF cations site population follows a pattern guided by mutual exclusions caused by short contacts. H_2O is distributed among six OW sites radiating from the axis of the cavity.

In the recent years, the analysis of the thermal stability of erionite has received some interest (Bish, 1989; Bish and Carey, 2001; Ballirano and Cametti, 2012; Ballirano and Pacella, 2016; Ballirano et al., 2018). Many of those investigations were performed with the aim of disclosing details of the EF cations mobility to be exploited for a deeper knowledge of the possible ion-exchange processes possibly occurring after inhalation of erionite fibers. In fact, due to several investigations of the health effects in humans of erionite inhalation, this zeolite has been classified as a Group-I carcinogen by the International Agency for Research on Cancer (IARC, 1997). Ballirano et al. (2018) have observed that erionite shows a direct dependence of the temperature of breakdown (T_{break}) from the Si/Si+Al ratio and an inverse one of the temperature of dehydration (T_{dehydr}). The dependence of thermal stability from the weighted ionic potential $(Z/r)_{wt}$, proposed by Cruciani (2006) does not hold for the analyzed samples suggesting that not only chemistry but also the position where EF cations are allocated within the erionite cage plays a relevant role in modulating such property.

The recent characterization of a K-exchanged sample (Pacella et al., 2017), prepared for investigating possible (partial) inactivation routes of the fibers, has produced interesting results. In fact, despite having completely occluded all available pores with K ions, erionite preserved the capability to upload Fe (II) within the erionite cage. Fe (II) has been claimed to be one of the factors potentially able to induce genotoxicity by Fenton chemistry (Fubini and Mollo, 1995).

Owing to the peculiarity of the EF cation content of this sample, it is of interest to analyze its thermal stability the aim being to provide relevant information for modeling the thermally induced behavior of the erionite group. The present work analyzes the structural modification occurring upon heating by *in situ* high-temperature X-ray powder diffraction (HT-XRPD) and thermogravimetric and differential scanning calorimetry (TG/DSC).

EXPERIMENTAL

Enrichment of the raw sample was carried out according to the protocol of Ballirano and Cametti (2015). The enriched pristine material was erionite-Na from Rome, Oregon, USA fully characterized by Ballirano et al. (2015) and having the crystal chemical formula $[Na_{3.8(3)}K_{2.5(3)}Mg_{0.42(17)}][Al_{7.24(11)}Si_{28.76(11)}O_{72.10(14)}]\cdot 29.60H_2O$. The K-exchange process was performed following the procedure described by Pacella et al. (2017) producing a sample of crystal chemical formula $[Na_{1.41(10)}K_{5.91(9)}Mg_{0.44(7)}][Al_{7.49(5)}Si_{28.51(5)}O_{72.35(4)}]\cdot 30.73H_2O$. H_2O content was not measured by the authors but calculated hypothesizing water content of 18.5 wt.%. The slightly different Si/Si+Al ratio calculated from the two analyses (0.792 vs 0.799) may be attributed to experimental error.

In the present work, the weight change and the energetic transformations were evaluated on both pristine and K-exchanged samples by simultaneous Differential Scanning Calorimetry and Thermogravimetric Analysis (DSC/TG: Netzsch STA 449 C Jupiter). During DSC/TG analysis the samples were heated at a rate of 10 K min^{-1} in the 297-1273 K temperature range (1473 K for pristine sample) under an air flow of 30 mL min^{-1}. Approximately 20 mg of sample was used for each run of both pristine and K-exchanged samples and experiments were carried out in triplicate. Instrumental precision was checked by three repeated collections on a kaolinite reference sample revealing good reproducibility (instrumental theoretical T precision of ±1.2 °C). Derivative thermogravimetry (DTG) and Derivative Differential Scanning Calorimetry (DDSC) were obtained using Netzsch Proteus thermal analysis software.

A qualitative phase analysis of the samples recovered from thermogravimetric analyses was performed by XRPD using a Bruker D8 Advance X-ray diffractometer operating in reflection mode at 40 kV and 40 mA. Scans

were recorded in the range of 3-66 °2θ, with a step size of 0.02 °2θ and a counting time of 3 s. Mineral phases were identified using DIFFRAC plus EVA software, by comparing the experimental peaks with reference patterns stored in the 2005 PDF2. For HT-XRPD an aliquot of powder was loaded and packed in a 0.7 mm diameter SiO_2-glass capillary, open at both ends. It was entrapped between two flocks of high-temperature insulating wool, lying at both ends of the capillary to avoid any axial displacement of the powder during measurements and to permit H_2O evacuation. The capillary was glued to a 1.0 mm diameter Al_2O_3 tube using alumina ceramic. Diffraction data were acquired using a focusing-beam Bruker AXS D8 Advance. The instrument operates in transmission mode, in θ-θ geometry, and is fitted with a capillary heating chamber and a PSD VÅntec-1. Details of thermocouple calibration are reported in Ballirano and Melis (2007).

A magnified view of the full data set is reported in Figure 1 under the form of a pseudo-Guinier plot. Preliminary scrutiny of the data indicated the occurrence of ca. 2.5 wt% of chabazite ($Ca_2Al_4Si_8O_{24}\cdot 12H_2O$) and traces of quartz (<0.1 wt.%). Moreover, a content of <<5 wt% of nontronite was estimated.

Rietveld refinements (Rietveld, 1969) were carried out using TOPAS V.4.2 (Bruker AXS, 2009) using the mixed Rietveld/Pawley method described in Ballirano and Cametti (2015). Starting structural data of K-exchanged erionite were taken from Pacella et al. (2017) whereas those of chabazite and quartz from Yakubovich et al. (2005) and Le Page and Donnay (1976), respectively. Only cell parameters were refined for chabazite and quartz. No restraints on bond distances and angles were imposed during the structure refinement of K-exchanged erionite. As in previous HT investigations of erionite samples, displacement parameters were constrained as $B_{T1}=B_{T2}$; $B_{O1}=B_{O2}=B_{O4}$; $B_{O3}=B_{O5}=B_{O6}$; $B_{K1}=B_{K2}$; $B_{Ca1}=B_{Ca2}=B_{Ca3}=B_{Ow8}=B_{Ow9}=B_{Ow10}=B_{Ow11}=B_{Ow12}=2*B_{Ow7}$ because of the existence of correlations. Absorption was corrected following the Sabine (1998) approach for cylindrical samples. Preferred orientation was modelled by spherical harmonics (six refinable parameters up to the 8th order). The number of terms was selected using the procedure devised by Ballirano (2003).

A first series of refinements was performed freely optimizing the whole set of parameters. Subsequently, a second series of refinements was performed keeping fixed the isotropic displacement parameters to the corresponding values obtained from linear fittings of the values obtained in the first series of refinements. The final series of refinement was obtained keeping the spherical harmonics terms fixed to the corresponding averaged values (y20=0.082; y40=0.017; y60=0.000; y66p=0.008; y80=-0.009; y86p=0.000). The effect of the application of those restraints on the conventional disagreement indices Rp and Rwp was very small (increase <5%).

Examples of Rietveld plots of the data collected at 303 and 1143 K are shown in Figure 2, experimental details and miscellaneous data of the refinements are reported in Table 1. Structural data at each temperature are deposited at the journal site under the form of a multi-block CIF file.

RESULTS AND DISCUSSION

Thermogravimetric analyses of pristine and K-exchanged samples are reported in Figure 3. As can be seen a maximum mass loss of ca. 16% has been recorded for the pristine sample, a value that reduces to ca. 14% in the case of the K-exchanged sample (Table 2). This reduction confirms the hypothesis that the ion exchange process produces a partial segregation of K ions at sites occupied by H_2O in the pristine sample. More than 95% of the mass loss occurs in the 297-773K thermal range.

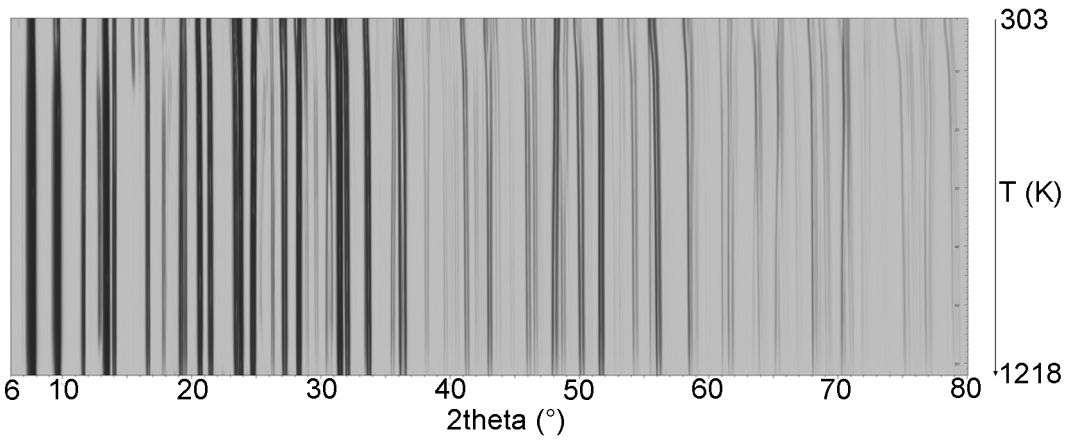

Figure 1. Magnified pseudo-Guinier plot (6-80° 2θ) of the full data set of the 303-1218 K heating run of K-exchanged erionite.

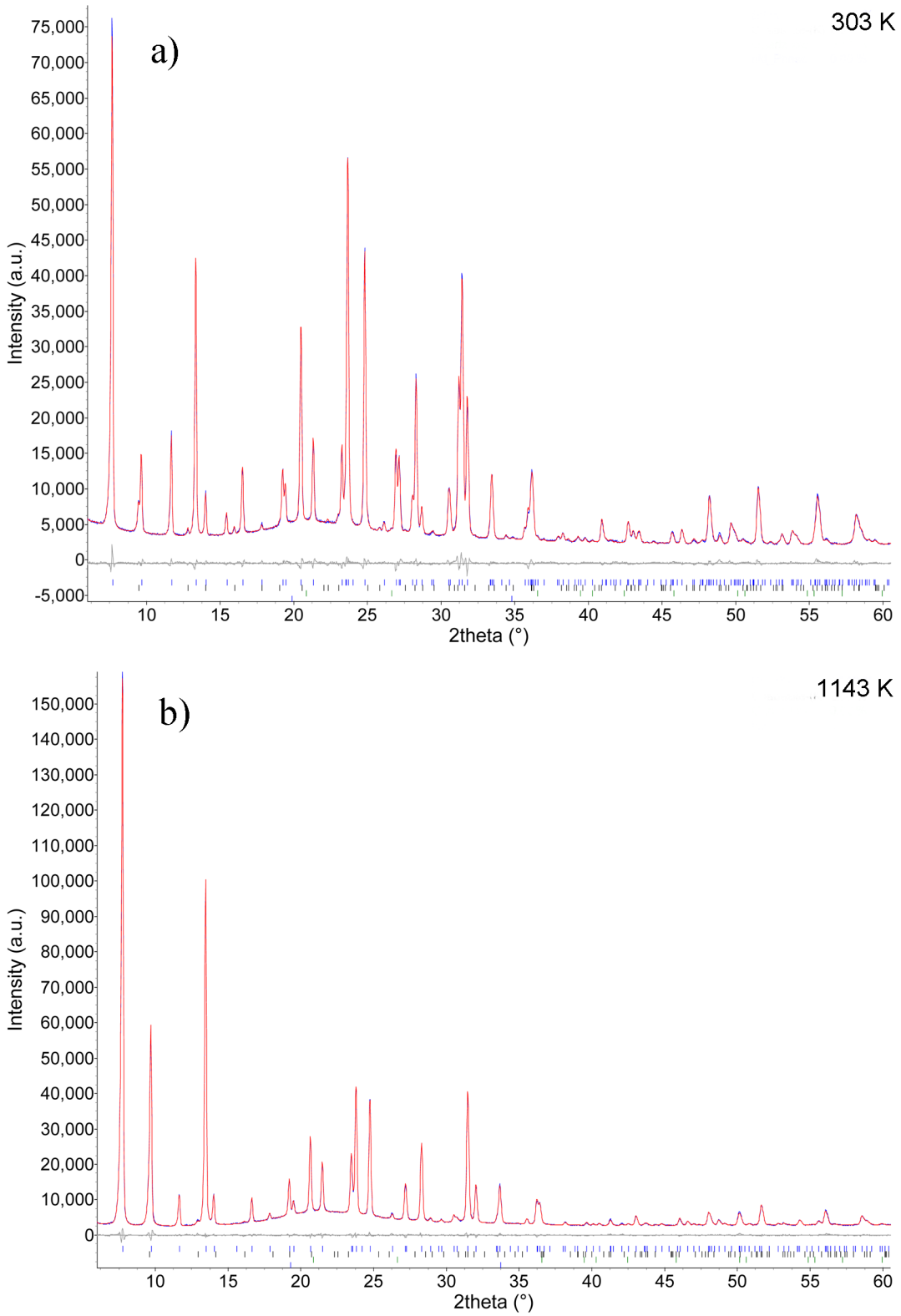

Figure 2. Magnified view (6-60° 2θ) of the Rietveld plots of the data collected at a) 303 K and b) 1143 K. The grey curve (below) represents the difference between observed and calculated plots. Vertical bars mark the position of calculated Bragg reflections of, from above to below: erionite, chabazite, quartz, and nontronite.

Table 1. Crystal data, experimental set-up, data collection details, and statistical indicators of the Rietveld refinements. Chemical data taken from Pacella et al. (2017) modified from thermal analysis carried out in the present work. Conventional disagreement indices as defined in Young (1993).

Chemical formula	$(Na_{1.41}K_{5.91}Mg_{0.44})[Al_{7.49}Si_{28.51}O_{72.35}]\cdot 24.80H_2O$
R=Si/(Si+Al)	0.792
Space group	$P6_3/mmc$
Cell parameters at 303 K (Å)	a=13.21672(7) c=15.07704(11)
Cell volume at 303 K (Å^3)	2280.84(3)
Instrument	Bruker-AXS D8Advance
X-ray tube	Cu operating at 40 kV and 40 mA
Incident beam optics	60 mm multilayer (Göbel) X-ray mirror
Sample mount	Rotating capillary (60 r/min)
Soller slits	2:2.3° incident beam; radial diffracted beam
Divergence slit	0.6 mm
Detector	PSD VÅNTEC-1
Thermal range (K)	303-1218
Temperature step (K)	15
Re-equilibration time at each T (s)	60
Thermal stability (K)	±1
Data range (°2θ)	6-145
Step size (°2θ)	0.022
Counting time (s)	2
wRp (%)	1.95-3.20
Rp (%)	1.51-2.35
R_{Bragg} (%)	0.40-1.07

The pristine sample shows three DTG maximum loss rate at 377, 427 and 573 K, the latter being weak, all related to different dehydration steps, which were also clearly recorded on DSC curve (Table 3). Finally, the strong endothermic peak at 1441 K signals the melting of the assemblage (visually checked).

The K-exchanged sample is characterized by a strong DTG maximum loss rate at 353 K and a weak one at 430 K which were due to dehydration steps of the sample as confirmed also by the two endothermic peak at 356 and 429 K on DSC curve (Table 3). The maximum temperature of the experiment was limited to 1273 K in order to avoid possible damages to the crucible as a result of melting. All DSC curve of both pristine and K-exchanged samples exhibit a weak exothermic effect in the range 1073-1223 K (Table 3) due to the thermal behavior of chabazite and nontronite (Grim and Rowland, 1942; Passaglia, 1970; Földvári, 2011) occurring as impurities in the samples. Moreover, in both samples, weak endothermic effects were detected on DDSC curves in the range 803-833 K arising from the structural α→β transition of quartz (Földvári, 2011; Bloise et al., 2016) which occurs in the samples as impurity.

The X-ray diffraction pattern of the pristine sample recovered after heating to 1273 K (Supplementary Figure 1) exhibits some reflections of erionite (39-1379 JCPDS card), quartz (46-1045 JCPDS card) and anorthite (20-0528 JCPDS card). In particular, almost all erionite reflections disappeared except for (100), (101), (110), (210) and (212) which were still visible, even if with greatly reduced intensity, suggesting that poorly crystalline erionite still persists after heating.

Moreover, XRPD showed a low amount of anorthite, deriving from chabazite breakdown/recrystallization as a result of heating up to 1273 K (Passaglia, 1970) and quartz present as impurities and deriving from nontronite breakdown (Földvári, 2011).

The X-ray diffraction pattern of the K-exchanged sample recovered after heating to 1273 K (Supplementary Figure 1) was characterized by sharp peaks, testifying the

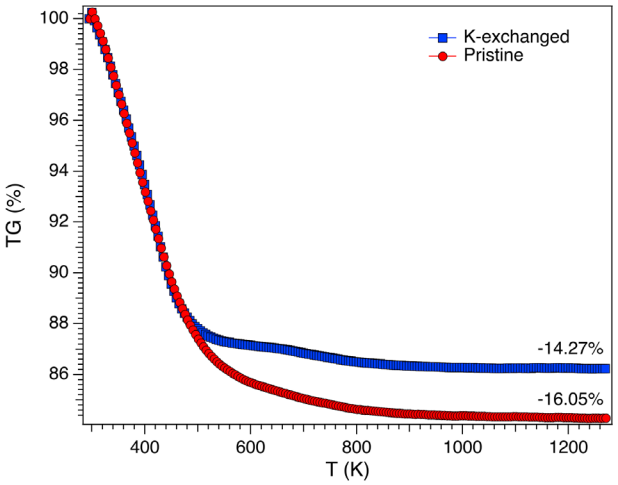

Figure 3. TG analyses of pristine and K-exchanged samples.

Table 2. Relevant TG data, mass loss %.

Thermal range (K)	297-383	297-773	297-1273
Pristine	5.43	15.70	16.05
K-exchanged	6.00	13.93	14.27

Table 3. Peak temperatures in DSC and DTG curves. w weak, s strong, endo endothermic, exo exothermic. * Average values calculated on three measures.

	*DSC (T/K)	*DTG (T/K)
Pristine	363 endo	377 s endo
	440 endo	427 endo
	576 w endo	573 w endo
	1118 exo	
	1441 endo	
K-exchanged	356 s endo	353 s endo
	429 w endo	430 w endo
	------	----
	1138 exo	

persistence of a high degree of crystallinity. The expected reflections caused by the presence of quartz and anorthite (arising from nontronite and chabazite breakdown) were not clearly apparent due to the overlapping with those of erionite.

The relative expansion of cell parameters and volume is graphically shown in Figure 4. No structural breakdown is observed within the analysed thermal range. As can be seen, the general behaviour is similar to that of the erionite-K sample analysed by Ballirano and Cametti (2012) characterized by a significantly higher R ratio. The *a*-parameter contracts marginally whereas the *c*-parameter suffers a still smaller expansion. The overall effect is a very small volumetric contraction quantified in a maximum volume contraction ΔV_{max} of 1.1%. Both *a*- and *c*-parameters show a small deviation except for a relatively smooth variation at ca. 440 K. Nevertheless, the relationships existing between R ratio and T_{break}, maximum compression along *a*- and *c*-axis, devised by Ballirano et al. (2018), do not apply to the present K-exchanged sample. An explanation of this apparently odd behaviour will be proposed below.

Minor chabazite collapses at 1143 K. The dependence of the *a*-parameter and α-angle (rhombohedral setting) from temperature is reported in Figure 5. The behaviour is very different with respect to pristine chabazite whose response to heating was analysed by Ballirano and Pacella (2016). In fact, the *a*-parameter smoothly decreases from ca. 9.38 Å at RT to ca. 9.30 Å at 528 K. At higher temperatures, the value remains constant up to 1068 K before a small contraction. It is possible to hypothesize that such contraction is related to the dehydration process that should be completed at 528 K. This value is reasonably close to 493 K reported for both chabazite-Na and -Ca (Cruciani, 2006). The α-angle reaches a maximum value of ca. 95.6° at 453 K before a regular decrease up to 888 K. The angle remains unchanged until 1038 K before experiencing a small increase. The dependence of volume from temperature (not shown) follows closely that of the a-parameter and results in a ΔV_{max} of 2.8% just before structure breakdown.

Differently from other analysed samples of erionite, microstrain e_0 (defined as $\beta_i = 4\varepsilon_0 \tan\theta$, where β_i = peak integral breadth: Ballirano and Sadun, 2009) is remarkably constant being 0.0671(4) throughout the investigated thermal range (value in parenthesis refers to the dispersion of the data).

Both <T1-O> and <T2-O> bond distances show a marginal contraction (Figure 6) that is due to the effect of thermal vibrations. In fact, application of a simple rigid body SRB correction (Downs et al., 1992) removes such effect, in particular for <T2-O>, resulting in $<T1\text{-}O>_{SRB}$ and $<T2\text{-}O>_{SRB}$ of 1.641(2) Å and 1.633(2) Å, respectively, to be compared to uncorrected <T1-O> and <T2-O> of 1.633(2) Å and 1.620(4) Å, respectively. Those data are in reasonable agreement with those reported at RT by Pacella et al. (2017) for K-exchanged erionite.

T-O-T angles show relatively small variations, confined in the 2-5° angular range, except for T2-O6-T2 that increases from ca. 171° at RT to ca. 177° at 423 K and remaining substantially unchanged at higher temperatures (Figure 7). The relatively minor variations testify that the

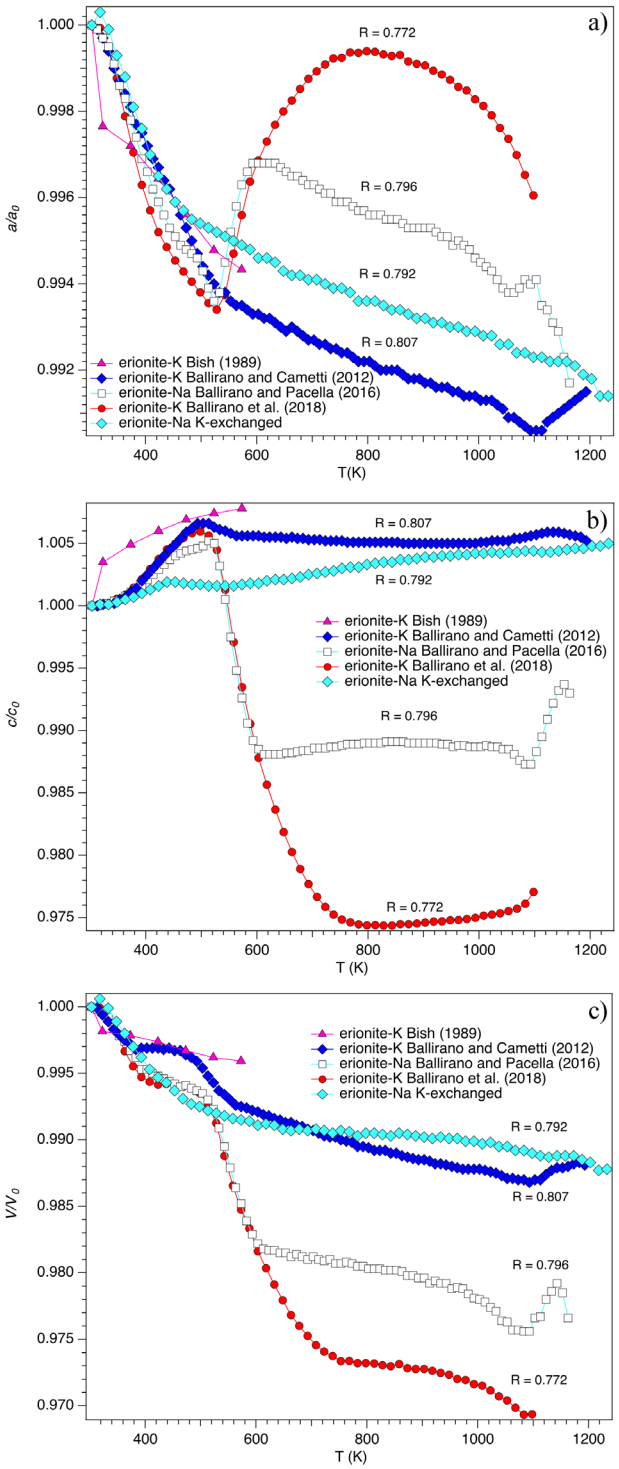

Figure 4. Relative expansion of a) *a*-, b) *c*-parameter and c) volume of woolly erionite-K in the 303-1218 K thermal range. For comparison purposes, data of Bish (1989), Ballirano and Cametti (2012), Ballirano and Pacella (2016) and Ballirano et al. (2018) are also reported. Erionite-K analysed by Bish (1989) was characterized by an R ratio of 0.785 (Sheppard and Gude, 1969) and was dehydrated *in vacuo*.

framework does not suffer relevant modifications upon heating.

At RT, EF cations are allocated at the Ca2, Ca3, K1, and K2 sites plus additional 2 atoms per formula unit (*apfu*) K disordered near or at sites commonly occupied by H_2O (OW sites) as indicated by Pacella et al. (2017). Upon heating, there is a progressive emptying of the Ca2 and Ca3 sites (Figure 8). In particular, the almost complete removal of site scattering *(s.s.)* at Ca3 is attained at 498 K whereas Ca2 experiences a strong reduction of *s.s.* from ca. 26 e^- at RT to ca. 8 e^- at 633 K. The *s.s.* remains

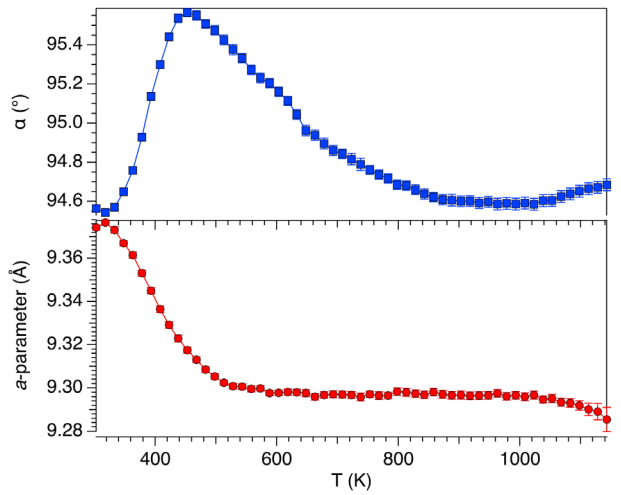

Figure 5. Evolution with temperature of the *a*-parameter and α-angle (rhombohedral setting) of admixed chabazite.

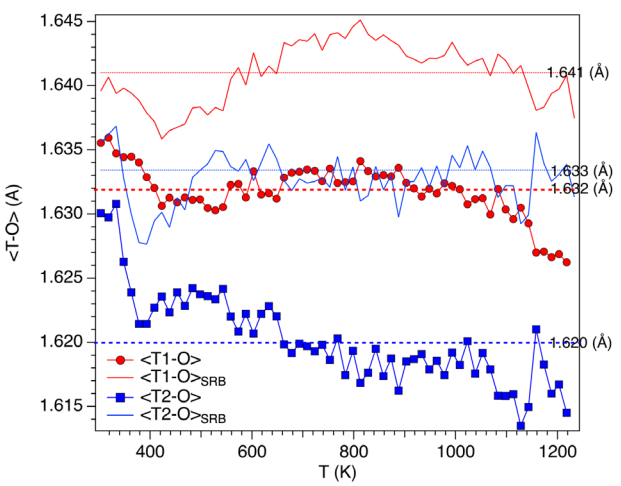

Figure 6. Evolution with temperature of <T1-O> and <T2-O>. Data corrected for simple rigid body model (Downs et al., 1992) are indicated as $<T1\text{-}O>_{SRB}$ and $<T2\text{-}O>_{SRB}$. Straight dotted and dashed lines are guides for eyes indicating the mean values of corrected and uncorrected <T-O> bond distances (same colour code).

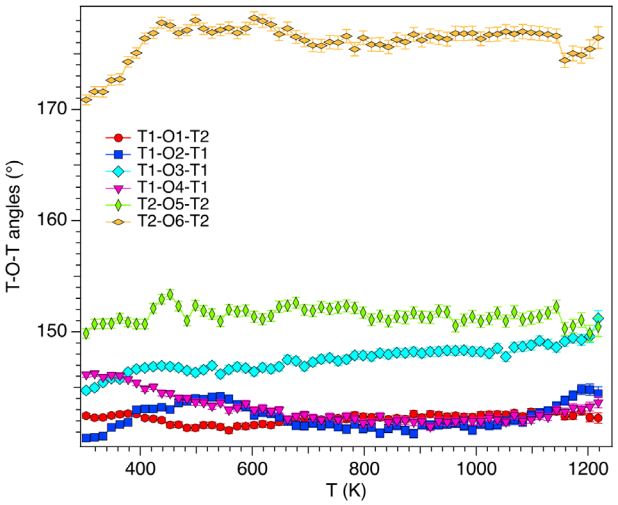

Figure 7. Evolution with temperature of the T-O-T bridges.

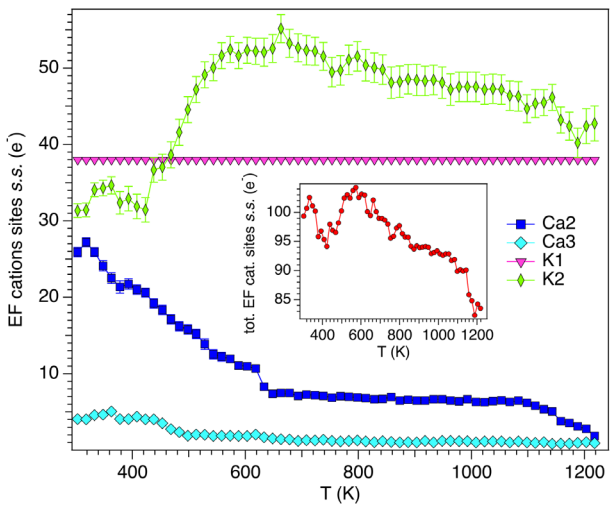

Figure 8. Evolution with temperature of the site scattering of the cation sites. Inset: dependence from temperature of the total site scattering of EF cation sites.

unchanged up to 1083 K before reducing quickly to 0 at 1218 K. The *s.s.* at K1 is unchanged throughout the analysed thermal range clearly indicating the absence of any "internal ion exchange" process (Schlenker et al., 1977). Differently, *s.s.* at K2 starts to increase at 438 K from ca. 31 e^- to a maximum value of 51 e^- that is reached at 573 K. At temperatures exceeding ca. 700 K the site starts emptying, at a slow rate, to a final value of ca. 43 e^-, that is reached at 1218 K. The increase of *s.s.* at K2 starts at a temperature that correlates with that of an endothermic peak observed in the DSC analysis of the sample. This fact suggests that the motion of K ions from OW sites is coupled with simultaneous dehydration. The inset of Figure 8 shows the evolution with temperature of the total s.s. observed at the EF cation sites. We notice a first reduction process reaching a minimum value at 423 K followed by a return back to approximately the same starting value at 513 K. At higher temperatures, the total s.s. restarts to decrease in a fairly smooth way up to ca. 83 e^- at 1218 K. This behaviour testifies a partial migration of the EF cations toward OW sites.

The occurrence and the extension of this process may be evaluated by the analysis of the thermally induced modification of the *s.s.* at the OW sites (Figure 9). Relatively high standard deviations associated to *s.s.* of sites OW9 and OW12 reflect the existence of correlations caused by their vicinity. As can be seen, a complete depletion of the H_2O sites is reached only by OW7 (618 K) and OW11 (663 K). Significant *s.s.* is, on the contrary, observed at the remaining four OW sites and OW9 and OW12 in particular. The sum of the *s.s.* at OW9 and OW12 regularly decreases to a minimum of ca. 57 e^- at ca. 500 K and then remains substantially constant a part of a spike at the last measured temperature. It is worth noting that this *s.s.* corresponds to ca. 3 *apfu* K. Following the same approach devised by Ballirano and Cametti (2012), based on the invariance of the EF cation content, the dependence from temperature of the total H_2O sites *s.s.* has been calculated. At RT ca. 25.5 H_2O per formula unit are calculated as compared to ca. 22 as observed from TG analysis. The corresponding curves show a reasonable agreement as far as the dependence from temperature is referred to (Figure 10). Accordingly, complete dehydration is attained at 663 K (i.e. the temperature at which OW11 becomes empty). T_{dehydr} is close to that

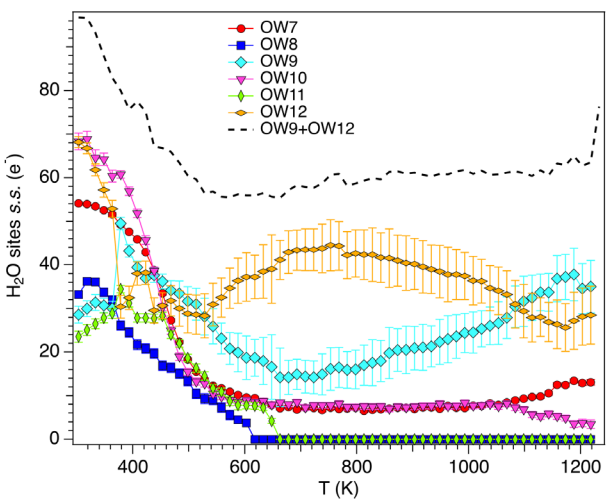

Figure 9. Evolution with temperature of the site scattering of the OW H_2O sites.

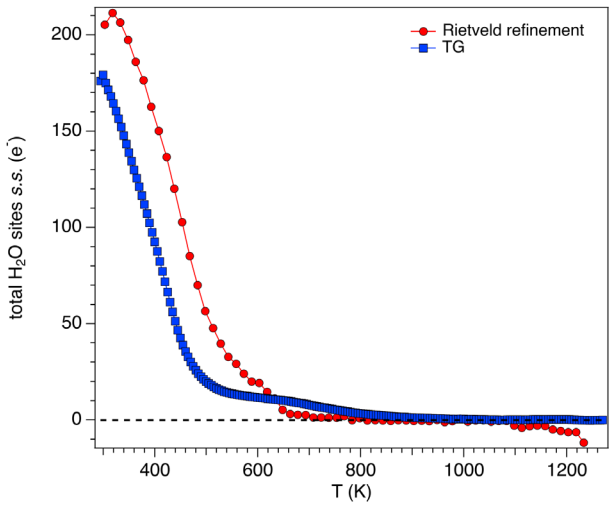

Figure 10. Comparison between the dependence from temperature of the total *s.s.* of OW H_2O sites after subtraction of the EF cations contribution and the *s.s.* of H_2O as recalculated from TG data.

observed by Ballirano et al. (2018) for erionite-K(Ca). It is worth noting that T_{dehydr} and T_{break} do not follow the dependence from R ratio indicated by Pacella et al. (2018) i.e. high Si content favours a lower T_{dehydr} and a higher T_{break}. This is possibly due to the effect of the relevant amount of large K ions dispersed within the erionite cage acting as reinforcing blocks for the framework. The stiffening effect is confirmed by the small contraction of the structure and the constancy of microstrain throughout the analysed thermal range. Having analysed in the recent years the thermal behaviour of a few samples of erionite characterized by different chemical compositions permits a detailed evaluation of the possible dependence of their thermal stability from weighted ionic potential $(Z/r)_{wt}$, proposed by Cruciani (2006). According to the data listed in Table 4 variation of this parameter seems to have little effect on T_{break}. According to the findings of present work the absence of correlation is reasonable as not only the typology of the EF cation plays an important role but also its location.

Like erionite-Na (Ballirano and Pacella, 2016), the *z* fractional coordinate of Ca3 (x=1/3, y=2/3) migrates from ca. 0.70 at RT to special position ¾ at 483 K i.e. the centre of the erionite cavity. However, this migration occurs at a higher temperature than that of erionite-Na which is of 423 K. Differently, the behaviour of the *z* coordinate of Ca2 (x=1/3, y=2/3) is different with respect to that reported for other erionite samples. In fact, it remains remarkably constant at 0.103(6) before experiencing a displacement toward 0.06 at temperatures exceeding 1158 K (value in parenthesis refers to data dispersion). The final displacement correlates with the complete depletion in terms of *s.s.* of the site.

As far as the evolution with temperature of the position of the OW sites is referred to, OW7, OW9, OW10, and OW12 are those characterized by the more relevant displacements. The OW7 migration towards the walls of the erionite cage is similar, albeit less pronounced than that observed in both erionite-K (Ballirano and Cametti, 2012) and erionite-Na (Ballirano and Pacella, 2016) passing from x=0.2385(4) at 303 K to x=0.229(2) at 1233 K (y=2x). This migration correlates with the progressive reduction of *s.s.* at the site. The displacement is already completed at 528 K. OW9 shows a relevant displacement of the x coordinate (y=2x) from ca. 0.40 at RT to ca. 0.46 at 513 K and a strong *z* migration from ca. 0.94 to ca. 1.00 which occurs in the small 303-378 K thermal range. A very similar behaviour is shown by OW10 [x from ca. 0.42 to ca. 0.46 (y=2x); *z* from ca. 0.64 to special position 0.75] but the completion of the displacement occurs at a higher temperature (603 K). As in the case of OW7 migration correlates with the progressive reduction of *s.s.* at the site. OW12 suffers an abrupt migration at 378 K from x (y=2x) ca. 0.46 to ca. 0.51 and *z* from ca. 0.02 to 0.04. This phenomenon is synchronous with the sudden reduction of *s.s.* at the site from 70 to ca. 30 e^-. However, as above mentioned, caution should be used when evaluating the mutual behaviour of OW9 and OW12

Table 4. Temperature of dehydration (T_{dehydr}) and of structural breakdown (T_{break}) of erionite samples. $(Z/r)_{wt}$ refers to the weighted ionic potential as described in Cruciani (2006).

				T_{dehydr} (K)	T_{break} (K)	
Sample	Reference	R	$(Z/r)_{wt}$	End	Start	End
Erionite-K	Ballirano and Cametti (2012)	0.807	0.096	573	1113	1193
Erionite-Na	Ballirano and Pacella (2016)	0.796	0.090	600	1063	1173
Erionite-K(Ca)	Ballirano et al. (2018)	0.772	0.090	658	1053	1158
Erionite-Ca(K)	Cruciani (2006)	0.75	0.10	<673	<1023	
Erionite K-exchanged	Present work	0.792	0.084	663	>1218	

owing to correlations.

All those rearrangements arising within the erionite cavity are clearly attributable to the progressive onset of dehydration and the corresponding migration of EF cations toward OW sites. As indicated by Pacella et al. (2017) at RT approximately 2 *apfu* K are allocated at OW and H_2O loss imposes a migration toward the walls of the erionite cavity in order to obtain a favourable coordination to O atoms of the framework.

CONCLUSIONS

The thermal stability and dehydration dynamics of a K-exchanged erionite sample have been investigated by coupling derivative thermogravimetry and differential scanning calorimetry with *in situ* X-ray powder diffraction. The K-loading of the erionite sample was previously performed by Pacella et al. (2017) in order to prevent the Fe (II) binding process in erionite fibres, occluding all available pores by large potassium ions. Surprisingly, the K-doped sample preserved its ability to upload Fe (II) within the erionite cage. Since the peculiarity of the EF cation content of this sample, the investigation of its thermal stability is relevant for expand knowledge on the behavior of the erionite group upon heating. In fact, this work is part of a broader study, performed by the same research group, on the thermal stability of various erionite species: erionite-K (Ballirano and Cametti, 2012), erionite-Na (Ballirano and Pacella, 2016), erionite-K(Ca) (Ballirano et al., 2018).

The investigated sample showed a dependence of cell parameters and volume form temperature similar to that observed for erionite-K (Ballirano and Cametti, 2012): a reduction of the *a*-parameter and a small expansion of the *c*-parameter leading, as a net result, to a cell volume contraction. However, the dependence of T_{dehydr} and T_{break} with the Si/Si+Al ratio reported for zeolites (Ballirano et al., 2018) was not here observed, likely due to the high content of large K ions within the erionite cage acting as reinforcing blocks for the framework. In addition, results of this work confirmed no correlation between T_{break} and weighted ionic potential $(Z/r)_{wt}$. Heating produces the migration toward K2 of both EF cations allocated at Ca sites and K ions allocated at OW sites during the dehydration process. Interestingly, the general mobility of EF cations toward the walls of the erionite cage, in order to receive a suitable coordination by the oxygen atoms of the framework, was already observed in erionite samples showing different chemistry (Ballirano and Cametti, 2012; Ballirano and Pacella, 2016; Ballirano et al., 2018). Notably, the cation mobility of erionite has been supposed to play a primary role in the interactions with the biological environment. In particular, erionite toxicity has been attributed to its ability to bind iron within the structure by ion-exchange, which is a pre-requisite for reactive oxygen species generation (Eborn and Aust, 1995; Carr and Frei, 1999; Fach et al., 2003). On this basis, current findings can be helpful in shedding light on the pathogenic mechanisms of erionite.

ACKNOWLEDGEMENTS

The research was funded by Sapienza Università di Roma.

REFERENCES

Alberti A., Martucci A., Galli E., Vezzalini G., 1997. A reexamination of the crystal structure of erionite. Zeolites 19, 349-352.

Ballirano P., 2003. Effects of the choice of different ionisation level for scattering curves and correction for small preferred orientation in Rietveld refinement: the $MgAl_2O_4$ test case. Journal of Applied Crystallography 36, 1056-1061.

Ballirano P., Andreozzi G.B., Dogan M., Dogan A.U., 2009. Crystal structure and iron topochemistry of erionite-K from Rome, Oregon, U.S.A. American Mineralogist 94, 1262-1270.

Ballirano P. and Cametti G., 2012. Dehydration dynamics and thermal stability of erionite-K: Experimental evidence of the "internal ionic exchange" mechanism. Microporous and Mesoporous Materials 163, 160-168.

Ballirano P. and Cametti G., 2015. Crystal chemical and structural modifications of erionite fibers leached with simulated lung fluids. American Mineralogist 100, 1003-1012.

Ballirano P. and Melis E., 2007. Thermal behaviour of b-anhydrite $CaSO_4$ to 1,263 K. Physics and Chemistry of Minerals 12, 289-295.

Ballirano P., Merlino S., Bonaccorsi E., Maras A., 1996. The crystal structure of liottite, a six-layer member of the cancrinite group. Canadian Mineralogist 34, 1021-1030.

Ballirano P. and Pacella A., 2016. Erionite-Na upon heating: dehydration dynamics and exchangeable cations mobility. Scientific Reports 6, 22786.

Ballirano P., Pacella A., Bloise A., Giordani M., Mattioli M., 2018. Thermal stability of woolly erionite-K and considerations about the heat induced behaviour of the erionite group. Minerals, 8, 28. doi:10.3390/min8010028www.mdpi.com/journal/minerals.

Ballirano P., Pacella A., Cremisini C., Nardi E., Fantauzzi M., Atzei D., Rossi A., Cametti G., 2015. Fe (II) segregation at a specific crystallographic site of fibrous erionite: a first step toward the understanding of the mechanisms inducing its carcinogenicity. Microporous and Mesoporous Materials 211, 49-63.

Ballirano P. and Sadun C., 2009. Thermal behavior of trehalose dihydrate (Th) and β-anhydrous trehalose (Tβ) by in-situ laboratory parallel-beam X-ray powder diffraction. Structural chemistry 20, 815-823.

Bish D.L., 1989. Determination of dehydration behaviour of

zeolites using Rietveld refinement and high-temperature X-ray diffraction data. Geological Society of America Annual Meeting, Abstracts with Programs, 21, A73.

Bish D.L. and Carey J.W., 2001. Thermal properties of natural zeolites. In Natural zeolites: Occurrence, properties, applications. (Eds.): D.L. Bish and D.W. Ming, Reviews in Mineralogy and Geochemistry, Mineralogical Society of America, Chantilly, Virginia, 45, 403-452.

Bloise A., Catalano M., Barrese E., Gualtieri A.F., Gandolfi N.B., Capella S., Belluso E., 2016. TG/DSC study of the thermal behaviour of hazardous mineral fibres, Journal of Thermal Analysis and Calorimetry 123, 2225-2239.

Bruker AXS, 2009. Topas V.4.2: General profile and structure analysis software for powder diffraction data. Bruker AXS, Karlsruhe, Germany.

Carr A. and Frei B., 1999. Does vitamin C act as a pro-oxidant under physiological conditions? The FASEB Journal 13, 1007-1023.

Coombs D.S., Alberti A., Armbruster T., Artioli G., Colella C., Galli E., Grice J.D., Liebau F., Mandarino J.A., Minato H., Nickel E.H., Passaglia E., Peacor D.R., Quartieri S., Rinaldi R., Ross M., Sheppard R.A., Tillmanns E., Vezzalini G., 1997. Recommended nomenclature for zeolite minerals; report of the Subcommittee on Zeolites of the International Mineralogical Association, Commission on New Minerals and Mineral Names. Canadian Mineralogist 35, 1571-1606.

Cruciani G., 2006. Zeolites upon heating: factors governing their thermal stability and structural changes. Journal of Physics and Chemistry of Solids 67, 1973-1994.

Downs R.T., Gibbs G.V., Bartelmehs K.L., Boisen M.B. Jr., 1992. Variations of bond lengths and volumes of silicate tetrahedral with temperature. American Mineralogist 77, 751-757.

Eborn S.K. and Aust A.E., 1995. Effect of iron acquisition on induction of DNA singlestrand breaks by erionite, a carcinogenic mineral fiber. Archives of Biochemistry and Biophysics 316, 507-514.

Fach E., Kristovich R., Long J.F., Waldman W.J., Dutta P.K., Williams M.V., 2003. The effect of iron on the biological activities of erionite and mordenite. Environmental International 29, 451-458.

Földvári M., 2011. Handbook of thermogravimetric system of minerals and its use in geological practice. (Eds.): T. Fancsik, Occasional papers of the Geological Institute of Hungary, Geological Institute of Hungary, Budapest, 213, 7-180.

Fubini B. and Mollo L., 1995. Role of iron in the reactivity of mineral fibers. Toxicology Letters 82-83, 951-960.

Gard J.A. and Tait J.M., 1973. Refinement of the crystal structure of erionite. In Proceedings of the Third International Conference on Molecular Sieves. (Ed.): J.B. Uytterhoeven, Leuven University Press, Leuven, Belgium, 1973, 94.

Gottardi G. and Galli E., 1985. Natural zeolites. Springer-Verlag, Heidelberg, xii + 409.

Grim R.E. and Rowland R.A., 1942. Differential thermal analyses of clay minerals and other hydrous materials. Report of investigations 85, 801-818.

Gualtieri A., Artioli G., Passaglia E., Bigi S., Viani,A., Hanson J.C., 1998. Crystal structure-crystal chemistry relationships in the zeolites erionite and offretite. American Mineralogist 83, 590-600.

IARC, 1997. IARC Monographs on the evaluation of the carcinogenic risk of chemicals to humans. Silica and some silicates 42, 225-239.

Kawahara A. and Curien H., 1969. La structure crystalline de l'érionite. Bulletin de la Société Française de Minéralogie et de Cristallographie 92, 250-256.

Le Page Y. and Donnay G., 1976. Refinement of the crystal structure of low-quartz. Acta Crystallographica B32, 2456-2459.

Meier W.M. and Groner M., 1981. Zeolite structure type EAB: crystal structure and mechanism for the topotactic transformation of the Na, TMA form. Journal of Solid State Chemistry 37, 204-218.

Pacella A., Cremisini C., Nardi E., Montereali M.R., Pettiti I., Ballirano P., 2017. The mechanism of iron binding processes in erionite fibres. Scientific Reports 7, 1319.

Pacella A., Cremisini C., Nardi E., Montereali M.R., Pettiti I., Giordani M. Mattioli M., Ballirano P., 2018. Different erionite series species are able to fix iron into the structure: implication for fibrous erionite toxicity. Minerals, 8, 36. doi:10.3390/min 8020036.

Passaglia E., 1970. Crystal chemistry of chabazites. American Mineralogist 55, 1278-1301.

Passaglia E., Artioli G., Gualtieri A., 1998. Crystal chemistry of the zeolites erionite and offretite. American Mineralogist 83, 577-589.

Rietveld H., 1969. A profile refinement method for nuclear and magnetic structures. Journal of Applied Crystallography 2, 65-71.

Rüdinger B., Tillmanns E., Hentschel G., 1993. Bellbergite - a new *mineral* with the structure type EAB. Mineralogy and Petrology 48, 147-152.

Sabine T.M., Hunter B.A., Sabine W.R., Ball C.J., 1998. Analytical expressions for the transmission factor and peak shift in absorbing cylindrical specimens. Journal of Applied Crystallography 31, 47-51.

Schlenker J.L., Pluth J.J., Smith J.V., 1977. Dehydrated natural erionite with stacking faults of the offretite type. Acta Crystallographica B33, 3265-3268.

Smith J.V. and Bennett J.M., 1981. Enumeration of 4-connected 3-dimensional nets and classification of framework silicates: the infinite set of ABC-6 nets; the Archimedean and 6-related nets. American Mineralogist 66, 777-788.

Smith J.V., Rinaldi F., Dent Glasser L.S., 1963. Crystal structures with a chabazite framework. II. Hydrated Ca-chabazite at room temperature. Acta Crystallographica 16, 45-53.

Staples L.W. and Gard J.A., 1959. The fibrous zeolite erionite: its occurrence, unit cell, and structure. Mineralogical Magazine 32, 261-281.

Wise W.S. and Tschernich R.W., 1976. The chemical compositions and origin of the zeolites offretite, erionite, and levyne American Mineralogist 61, 853-863.

Yakubovich O.V., Massa W., Gavrilenko P.G., Pekov I.V., 2005. Crystal structure of chabazite K. Crystallography Reports 50, 544-553.

Young R.A., 1993. Introduction to the Rietveld method: In: The Rietveld method. (Ed.): R.A. Young, Oxford University Press, Oxford, 1-38.